Accepted Article Preview: Published ahead of advance online publication

Femtosecond laser fabrication of black quartz for infrared photodetection applications

Raffaele De Palo, Annalisa Volpe, Pietro Patimisco, Andrea Zifarelli, Angelo Sampaolo, Antonio Ancona, Hongpeng Wu, and Vincenzo Spagnolo

Cite this article as: Raffaele De Palo, Annalisa Volpe, Pietro Patimisco, Andrea Zifarelli, Angelo Sampaolo, Antonio Ancona, Hongpeng Wu, and Vincenzo Spagnolo. Femtosecond laser fabrication of black quartz for infrared photodetection applications. *Light: Advanced Manufacturing* accepted article preview 5 March, 2025; doi: 10.37188/lam.2025.026

Received 26 September 2024; revised 26 February 2025; accepted 27 February 2025; Accepted article preview online 5 March 2025

FEMTOSECOND LASER FABRICATION OF BLACK QUARTZ FOR INFRARED PHOTODETECTION APPLICATIONS

Raffaele De Palo[1,2], Annalisa Volpe[1,2*], Pietro Patimisco[1,3,4], Andrea Zifarelli[1], Angelo Sampaolo[1,3,4], Antonio Ancona[1,2], Hongpeng Wu[3*], Vincenzo Spagnolo[1,3,4*]

[1]*Dipartimento Interateneo di Fisica, University of Bari and Polytechnic of Bari, Bari 70126, Italy*
[2]*CNR-IFN UOS Bari, Bari 70126, Italy*
[3]*State Key Laboratory of Quantum Optics and Quantum Optics Devices, Institute of Laser Spectroscopy, Shanxi University, Taiyuan 030006, China*
[4]*PolySenSe Innovations Srl, Via Amendola 173 Bari 70126, Italy*

*Corresponding author
annalisa.volpe@poliba.it
vincenzoluigi.spagnolo@poliba.it
wuhp@sxu.edu.cn

ABSTRACT

Quartz tuning forks have been recently employed as infrared photodetectors in tunable laser diode spectroscopy because of their high responsivities and fast response time. As for all sensitive elements employed for photodetection, the main drawback is the limited bandwidth of their absorption spectrum. For quartz crystals, the high absorptance for wavelengths above 5 µm guarantees excellent performance in the mid-infrared range, that cannot be easily extended in the visible/near-infrared range because of its transparency from 0.2 to 5 µm. In this work, we report on the development of a laser surface functionalization process to enhance the optical absorption of quartz crystals, named hereafter *Black Quartz,* in the 1-5 µm spectral range. *Black Quartz* consists of surface modification of quartz crystal by ultra-fast-pulsed-laser-processing to create localized matrices-like patterns of craters on top. The surface modification decreases the transmittance of quartz in the 1-5 µm range from > 95% down to < 10%, while the transmittance above 5 µm remains unchanged. The *Black Quartz* process was applied on two quartz-tuning-forks mounted in a tunable laser diode spectroscopy sensor for detecting two water vapor absorption features, one in the near infrared and the other one in the mid-infrared. A comparable responsivity was estimated in detecting both absorption features, confirming the extension of the operation in the near-infrared range. This works represents an important and promising step towards the realization of quartz-based photodetector with high and flat responsivity in the whole infrared spectral range.

INTRODUCTION

Detecting and sensing infrared radiation is extremely important in various applications, such as optical communication, imaging and spectroscopy.[1–4] Mature semiconductor technologies, such as silicon in 400-1100 nm, InGaAs in 800-1600 nm, and HgCdTe in 3-5 µm, dominate the infrared photodetector market. A proper semiconductor material can be selected to cover a specific spectral band with unmatchable sensitivity, but without the chance to efficiently operate outside it. In the last few decades, this scenario has motivated the scientific research to exploit advances in nanofabrication of low dimensional structures to address this issue, as well as to increase the performance, lower the cost, simplify the fabrication processes, and reduce the size. High responsivities have been achieved with InAs nanowires and carbon nanotubes but these solutions still present different challenges,[5–7] especially the one aimed at spectrally broadening their operation. Although different approaches have been proposed for 2D materials with encouraging results for broadband infrared photodetection,[8,9] the take-home message is that methodologies to be adopted for broadening the operating spectral range compromises ineluctably the responsivity of the sensing element in the whole sensing band. For example, graphene-based infrared photodetectors have gathered special attention due to their gapless band structure,[10] making them highly suitable for broadband detection, but

they are still characterized by low optical absorption which limits the ultimate responsivity.[11] In any case, photodetectors based on low dimensional structures are still far from mass production due to various issues, such as high output variability in material fabrication and processing,[9] that still need to be addressed.

A different approach can be identified in the surface and/or bulk modification of 3D-crystals to tailor their mechanical, electrical, and optical properties.[12–16] This strategy has been widely employed in photovoltaics applications, for enhancing the solar absorptance of photoconductive crystals. Many studies report on *Black Silicon,*[17–25] namely the enhancement of optical absorption of silicon in different spectral regions, from the visible to the far infrared range, through a surface functionalization of the crystal.

Ultra-fast pulsed laser processing represents one of the most promising techniques for tailoring the surface properties of a 3D-crystal. With respect to other methods based on photolithography or chemical etching, ultra-fast pulsed laser processing has various advantages: it is contactless, does not require pre-treatments or chemical processing of the crystal surface and its resolution is limited only by the depth of focus of the laser optics, with the potentiality to achieve fast processing over large areas.[26–28] This technique has been fully exploited in the surface texturing of diamond to extend and improve its optical absorption in the 0.2-2 μm spectral interval, still for photovoltaic applications.[29,30]

The idea behind this work is to use the same *blackening* approach widely used on silicon and on other photoactive mediums used for infrared photodetection, with the aim of extending the spectral range of the optical absorption over their natural absorption interval, without altering other figures of merit of photodetection, such as the responsivity and the response time. The optimal candidate is the quartz tuning fork (QTF), recently used as photodetector in tunable diode laser spectroscopy (TDLAS),[31–33] this technique is also known as light-induced thermoelastic spectroscopy (LITES).[34] The relevance of quartz as sensing element is strictly related to its piezoelectric properties. Several works have modelled the thermoelastic-piezoelectric phenomena for real cases, starting from various generalized thermoelasticity theories.[35–37] Photodetection in QTF is based on the thermoelastic conversion of absorbed radiation within the quartz in a polarization field, exploiting the piezoelectric nature of quartz.[38] The strong absorption at wavelengths greater than 5 μm allowed the achievement of responsivities up to 3 x 10^3 V/W.[39,40] The *blackening* approach could be used in this case to extend the absorption of quartz also for wavelengths below 5 μm, where this material is almost transparent, without altering the performance at longer wavelengths.
In this work, we report on the realization of *Black Quartz* through ultra-fast laser surface processing. A femto-second (fs) pulsed laser was used to create matrices-like patterns of round craters on the surfaces of quartz crystal wafers. These matrices patterns had the goal of make the quartz transmittance low and flat in the wavelength range of interest. Finally, a proof of concept was demonstrated through implementation of two laser-textured QTF as photodetector in a LITES setup for detection of two water vapor absorption features at 1.39 μm and 7.38 μm.

RESULTS

Optical absorption enhancement through superficial texturing

The crystalline α-quartz with z-cut has a direct bandgap at the Γ point equal to 6.3 eV, causing a high optical absorption at wavelengths λ shorter than 200 nm. For λ > 200 nm, the quartz remains highly transparent until the first high broadband absorption vibrational mode appears around 6 μm.[40] The transmittance spectrum of a 0.25 mm-thick z-cut α-quartz sample, with dimensions of 25.4 mm × 25.4 mm and a 2° rotation along the x-axis, is shown in Fig. 1. The spectrum was recorded in the near- and mid-infrared regions using a Nicolet iS50 Fourier transform spectrometer.

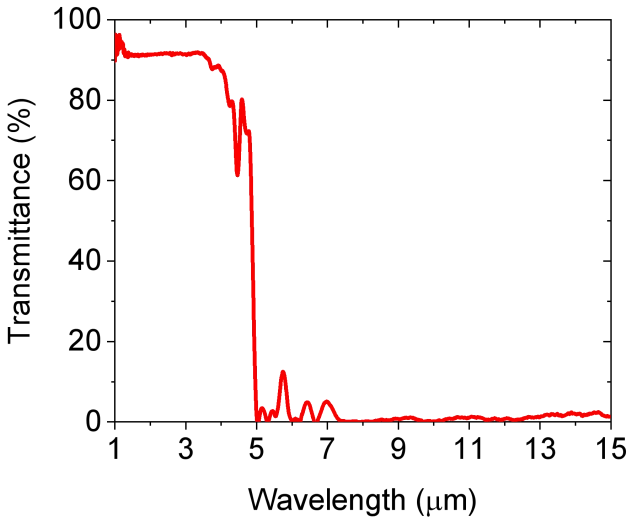

Fig. 1. Transmission spectrum of 0.25 mm-thick z-cut α-quartz.

The spectral dependence of the transmittivity in the range 1.0 – 15 μm shows a switching behaviour between transparency and opacity, with a sharp edge in the range 4–5 μm. At $\lambda > 5$ μm (named hereafter as the opaque region), the crystal is highly opaque meaning that all the electromagnetic infrared energy is deposited in the sample. Conversely, at $\lambda < 4$ μm (named hereafter as the transparent region), the optical properties change, and the quartz becomes highly transparent.

The enhancement of optical absorption in the near infrared range in a z-cut α-quartz has been obtained with surface micro structuring through irradiation by femtosecond (fs) laser pulses. The quartz was textured in ambient air with a pattern consisting of a localized matrix of ablated craters in an overall area of ~ 300 x 300 μm^2.

Since the surface texturization was performed in open air, the potential incorporation of nitrogen atoms into the laser-textured surfaces cannot be entirely ruled out.[41] To investigate this, an energy-dispersive x-ray analysis (EDX) analysis on both laser-textured quartz and pristine material was performed. The results showed no significant differences between the spectrum of the textured and pristine samples, indicating that, if any external species were incorporated into the sample, their concentrations were too low to be detected. This surface treatment creates an array of micro-structures, resulting in a strong modification of the optical absorption properties arising from various phenomena occurring simultaneously. For example, localized lattice rearrangements during texturing process create surface defects which in turn lead to the formation of additional energy levels within quartz band-gap region, creating new excitation pathways for the carriers from the valence band to the conduction band.[29,42] Other phenomena occurring in enhancement absorption could be attributed to changes and distortions of the material band structure, as well as creation of lattice structural defects.[43,44] Also, the change of morphology reduces the reflectance of light on the surface, enhancing light absorption via multiple surface-confined reflections.[18] This light trapping effect on the surface is significantly promoted and enhanced by craters dimension (~ 30 μm), which is one order of magnitude greater than the target wavelength (1-5 μm).[45,46]

Experimental optimization. The surface texturing of quartz was realized by designing localized matrices of craters using the setup shown in Fig.7 in the Materials and Methods section. A preliminary investigation was mandatory to establish the best operating conditions, namely the number *N* of laser pulses per crater and the centre-to-centre distance *h* between two consecutive craters. The values of laser fluence *F* (J/cm^2) and *N* were chosen in order to be well above the threshold ablation of quartz.[47] The craters were analysed by studying the diameter *D* and the depth *d* trends, both as function of the number of pulses *N*.

Seven matrices were realized with different combinations of *N* and *h*, to investigate different craters depth and density. The laser fluence and the laser repetition rate were fixed at F = 10 J/cm^2 and f_R = 60 kHz for all matrices. In Table 1, the working parameters for each matrix are listed, together with the diameters and depths of the corresponding craters. The results of the characterization, in terms of depths and diameters of the craters, are also reported in Figs. S1 a and b (supplementary information), respectively.

Table 1 *N* (number of pulses) and *h* (center-to center distance) combination for each matrix, with the corresponding crater diameters *D* and depths *d*.

Matrix	*N*	*h [µm]*	*D [µm]*	*d [µm]*
M1	10	100	27.10	2.33
M2	10	50	27.10	2.33
M3	10	35	27.10	2.33
M4	20	50	32.45	5.86
M5	50	50	35.93	14.98
M	100	50	36.22	19.95
M*	100	40	36.22	19.95

The optical transmission of each matrix was measured by using the setup reported in Fig. S2 (supplementary information) by employing five representative laser sources (Table S1 supplementary information) in the infrared range at the following wavelengths: 1.4 µm, 3.3 µm, 4.5 µm, 5.2 µm, 7.8 µm and 10.6 µm. With an area of approximatively 300 µm x 300 µm to be investigated, broadband light sources are not suitable because they cannot get a perfect collimation and a perfectly focused spot, since the focal spot size changes with the wavelength. The drawback is that some wavelengths might be focused on the textured area while others outside, compromising the reliability of the acquired spectrum. The optical transmission values are reported in Fig. S3 (supplementary information) as a function of the laser wavelength. For all matrices, the textured area does not alter the transmittivity of the quartz crystal for wavelengths longer than 5 µm, remaining always < 2%. Conversely, the surface texturing reduces the transmittivity at the shorter wavelengths. An absolute measurement of the spectral absorbance *A* of the textured area is not feasible because the dimensions of the textured area are too small to allow efficient use of an integrating sphere, which requires sample sizes of at least a few cm^2. However, useful insights can be drawn regarding the reflectance *R*. For pure quartz in the 1–5 µm spectral range, the reflectance is generally below 10%.[48] Moreover, it is well established in the literature that blackening the surface further reduces the material's reflectance.[45] According to the energy conservation law, the absorbance is related to the transmittance *T* through the relation $A=(1-T)-R$. Before texturing, *R* is significantly smaller than $(1-T)$ and can therefore be neglected. After texturing, *R* decreases even further and *A* increases, allowing *R* to be neglected once again. Consequently, $(1-T)$ can be used as a reliable parameter to quantify the increase in absorbance resulting from surface texturization.

The matrices M and M*, which have the higher crater density, showed the highest absorbance values with respect to pristine quartz. In Fig.2 are shown a representative cut-out of 2x2 craters of the textured areas (Fig. 2a,b) and the calculated *1-T* values (Fig.2).

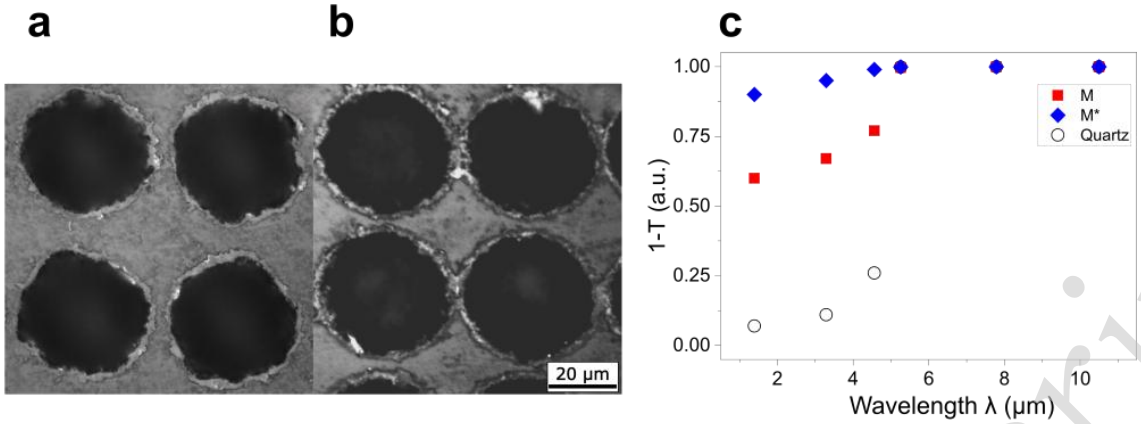

Fig. 2. Representative craters from matrix M (a) and matrix M* (b) 1-T spectrum of M, M* and pristine quartz.

M and M* were applied on two identical QTFs, having two prongs with length of 11 mm and thickness of 0.5 mm, separated by a spacing of 0.6 mm. They were realized starting from a double polished z-cut quartz wafers with a thickness of 250 µm, as those of the previous investigations,[49] using standard photolithographic techniques. The region of application of the two matrices was chosen in accordance with the working principles of QTF based photodetection.[34] When the radiation hits the surface of the QTF, photothermal energy is generated because of light absorption by the quartz. Due to the thermoelastic conversion, the photo-induced local heating creates elastic deformations that put prongs into vibration when the light is intensity-modulated at one of the QTF resonant frequencies. Thus, the induced strain field generates a local polarization, and charges appear on the surface of the QTF that can be collected by electrical contacts appropriately deposited along the QTF prongs. The strain field as well as the piezoelectric charges distribution are mainly localized at the prong clamped-end and for this reason the laser beam is focused near this region.[50] Therefore, the surface texturing has been realized in the form of localized matrices applied on the junction section between the clamped end of the prongs and the body of the QTFs, namely where the maximum strain occurs. A picture of the textured area applied to the two QTFs is shown in Fig. 3a and 3b. Hereafter, for ease of reading, the two textured QTFs will be referred to as the matrices applied to them, namely M-QTF and M*-QTF. The resonance curves of both QTFs were measured, before and after the laser texturing, to evaluate the impact of the laser texturing on the resonance properties of the QTF. A sinusoidal voltage excitation was provided to the QTF while the generated piezo-current was demodulated at the same excitation frequency by a lock-in amplifier. The resonances curves of M-QTF and M*-QTF were reconstructed by varying the excitation frequency, and the results are shown in Figs. 3c and 3d.

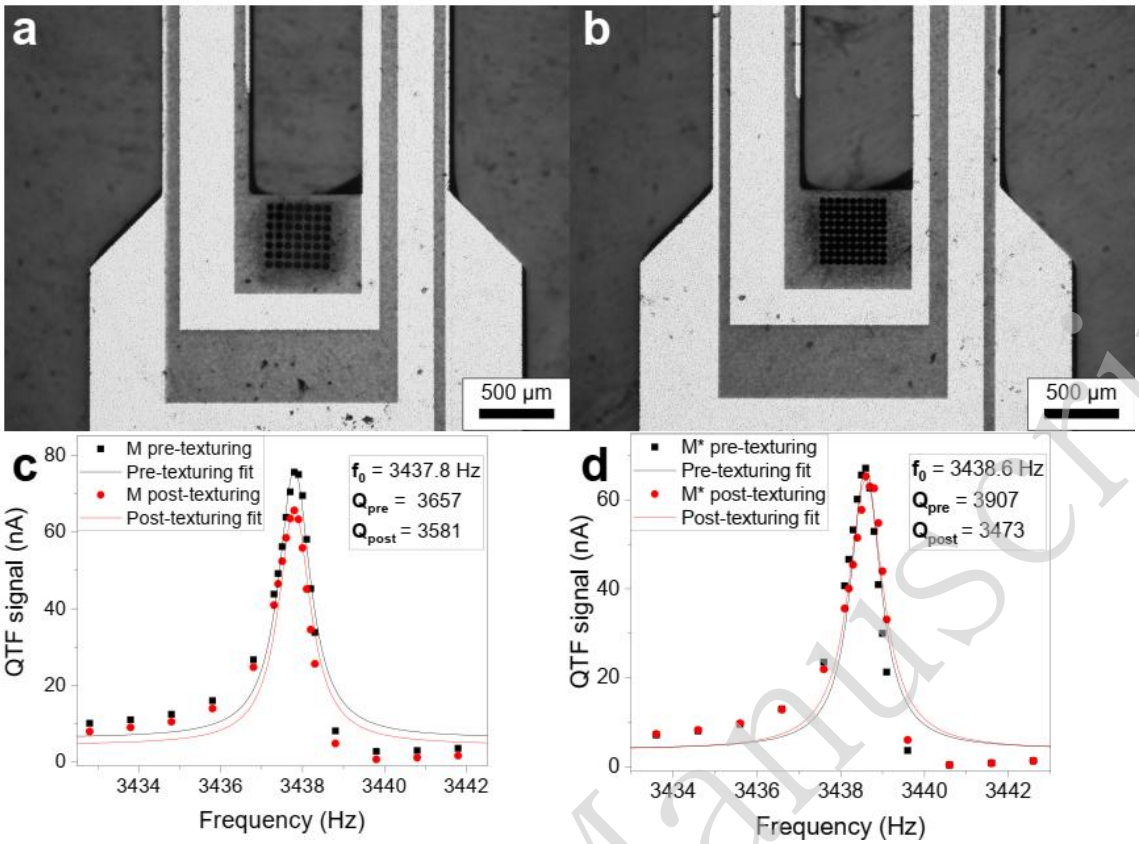

Fig. 3. Pictures of the two laser-textured QTFs M (a) and M*(b) together with their electrical response, (c) and (d), fitted with a Lorentzian function, before and after texturing.

Following the Butterworth–Van Dyke model, the equivalent circuit of a QTF can be modelled as an RLC circuit with a parallel stray capacitance (see Fig. 7a in the Materials and Method Section). The circuit analysis reveals that an increase in stray capacitance induces a right-left asymmetry relative to the peak value.[51] The data points were fitted with a Lorentzian function to retrieve both the resonance frequency and the quality factor (Q-value). No frequency shifts were observed in both cases. A negligible reduction of 3% in Q-value (from 3657 to 3581) was observed for M-QTF after the texturing, while the Q-value for M*-QTF dropped from 3907 to 3473 (11%) due to a higher density of craters, locally modifying the mechanical properties of the junction zone between the clamped prong end and the quartz support. This was expected because one of the loss mechanisms for a QTF is the interaction of the vibrating prong with the support,[52] which causes part of the mechanical vibrational energy of the prong to be lost by the support per each oscillation cycle. Altering the crystalline area in the junction with localized surface defects creates additional channels for dissipation, deteriorating the Q-value. However, a drop of 11% in the Q-value is expected not to significantly degrade the overall piezoelectrical properties of both QTFs.

QTFs as photodetector in a TDLAS setup for water detection. M-QTF and M*-QTF were used as a photodetector in a TDLAS setup for water vapor detection in air, at room temperature and atmospheric pressure, together with a bare QTF (named hereafter as B-QTF) with the same geometry as M-QTF and M*-QTF but without textured area, used as reference for highlighting the performance of the textured QTFs. The resonant frequency and the quality factor of B-QTF were measured equal to f_0 = 3441.1 Hz and Q = 4001. The schematic of the TDLAS setup is reported in Fig. S4 (supplementary information). The setup was assembled for accommodating two interchangeable sources, a diode laser (DL) targeting the water absorption line at 7194.80 cm^{-1} (1.39 µm) with an absorption cross-section of 1.73 x 10^{-22} cm^2 $molecule^{-1}$ and an optical power of 20 mW, and a quantum cascade laser (QCL) for the detection of the water line at

1354.83 cm^{-1} (7.38 µm) with an absorption cross-section of 3.30 x 10^{-21} cm^2 $molecule^{-1}$ and an optical power of 50 mW. The spectral profile of the cross-sections of both absorption features were simulated by using HITRAN database and reported in Fig. S5 (supplementary information). The DL emission falls within the transparent spectral region of the quartz, while the QCL in the opaque spectral region of the quartz (see Fig. 1). In this way, the effect of the texturing on the infrared photodetection in the transparent region could be analysed as well as the potential alteration of the performance in the opaque spectral range. After passing through an open pathlength of 10 cm, the laser beam was focused on the textured area of M-QTF or M*-QTF; for B-QTF the laser beam was focused on the same position as for textured QTFs. For both laser sources, the TDLAS sensor operated in wavelength modulation and *2f*-detection (*2f*-WM): the current driver was modulated at a half of the QTF resonance frequency and the acquired signal demodulated at the resonance frequency by means of a lock-in amplifier. A 10 mHz ramp signal was also superimposed to the current driver to linearly tune the wavelength emission and scan across the absorption feature. A room dehumidifier fixed the water concentration in the laboratory environment at 50% RH with a stable temperature of 19°C. The water vapor concentration was continuously monitored with a room hygrometer, and variations of ± 2% were recorded throughout the duration of all measurements reported hereafter. Such minor fluctuations are not significant enough to impact on the spectral reconstruction of the water vapor absorption line. Figure 4a reports the spectral scans of the water absorption line at 1.39 µm (using the DL) when the three QTFs were alternatively used, while Fig. 4b shows the *2f*-WM spectral scans detected at 7.38 (using the QCL) employing the same QTFs.

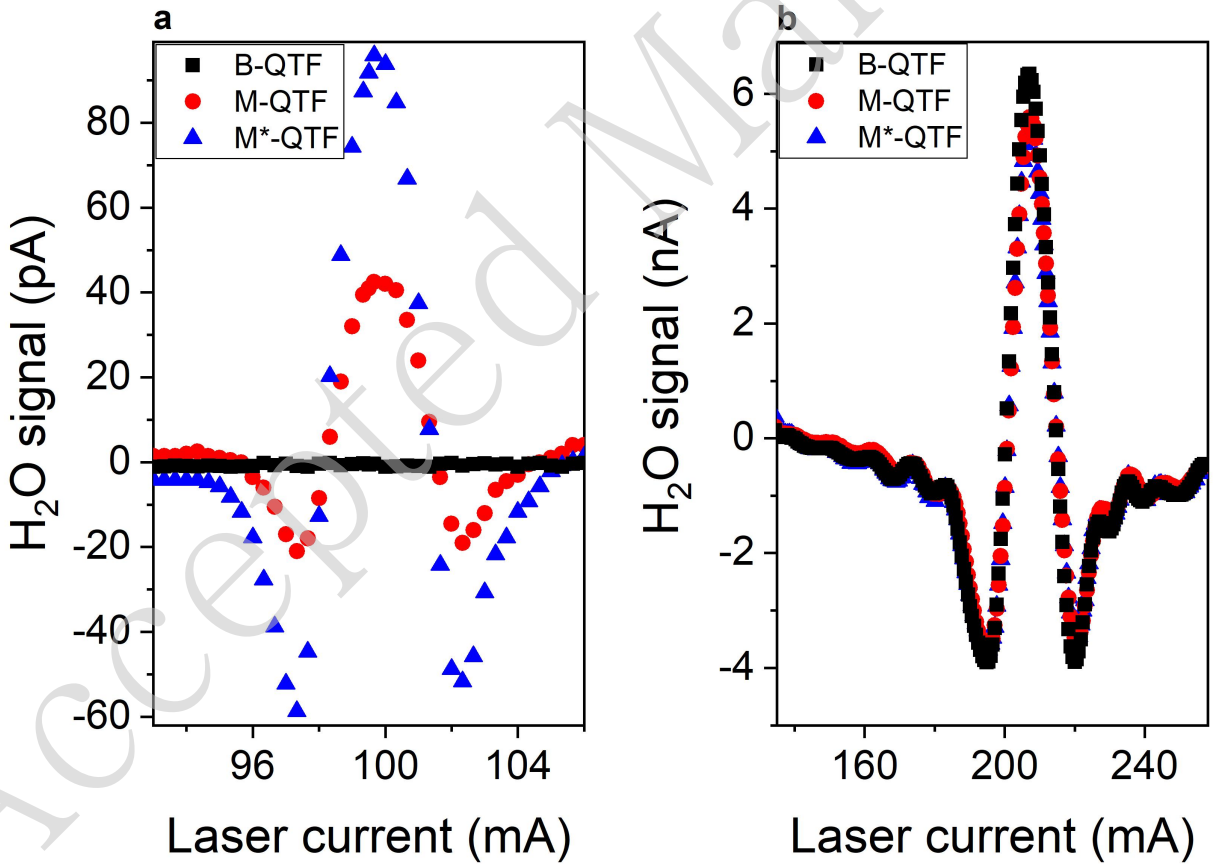

Fig. 4. (a) *2f* spectral-scans of water at 1.39 µm from B (black line), M (red line) and M* (blue line); (b) *2f* spectral-scans of water at 7.38 µm from B (black line), M (red line) and M* (blue line).

As expected, Fig.4a shows that no absorption feature was retrieved using B-QTF as photodetector because of the quartz transparency at 1.39 µm: the release of the optical energy in the quartz was too low for inducing localized thermoelastic effects. Conversely, the textured area in M-QTF and M*-QTF enabled the

surface optical absorption, and, in turn, the modulated optical energy was converted in resonant mechanical vibrational energy, generating a piezoelectric polarization field. The peak signals were used to estimate the responsivity of both textured QTFs at 1.39 µm, using the model proposed in the Methods Section. The responsivities R for M-QTF and M*-QTF at λ = 1.39 µm were R_M = 6.35 µAW^{-1} and R_{M^*} = 14.6 µAW^{-1}, respectively.

Figure 4b shows that, at 7.38 µm, the absorption feature of the water line was well reconstructed with the three QTFs. The peak signal retrieved with the B-QTF, equal to S_W = 6.35 nA, is only ~12% and ~16% higher than signals acquired with M-QTF and M*-QTF, respectively. These percentages are comparable with the values of the ratio between the Q factors of M and M* and that of B: Q_M/Q_B = 10% and Q_{M^*}/Q_B = 13%. The responsivity for M*-QTF at λ = 7.38 µm was estimated as 17.0 µAW^{-1}, comparable with the measurement at 1.39 µm (14.6 µAW^{-1}). The responsivity for M-QTF at λ = 7.38 µm was estimated as 19.0 µAW^{-1}. R_M at λ = 7.38 µm is three time its value at λ = 1.39 µm: this difference is related to a less efficient mechanism of thermoelastic conversion of M-QTF at lower wavelengths caused by its lower values of absorbance (see Fig.2c). Thus, two conclusions can be drawn: i) the texturing does not alter the performance of a QTF-based photodetector in the opaque spectral region; ii) the detector can be used both in the opaque and transparent spectral region with comparable performance, opening the way to a broadband infrared detection without a significant normalization due to spectral-dependence of the responsivity.

Analysis of the long-term stability

The long-term stability of the M*-QTF was studied through an Allan-Werle deviation analysis,[53] which related the noise level with the signal integration time, as described in the Methods section. The 7.38 µm-QCL was locked to 140 mA, far from the water absorption feature. The M*-QTF signal was acquired for three hours with an integration time t of 0.1 s. The results are shown in Fig.5.

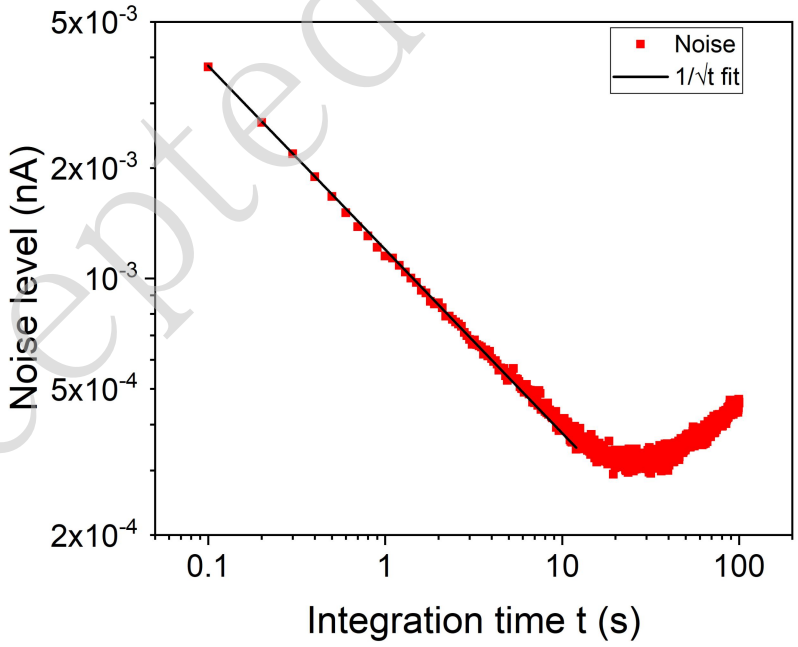

Fig. 5. Plot of M based sensor noise level as a function of integration time, determined using Allan-Werle deviation analysis, fitted with an inverse square root of t function.

The noise level decreased as the integration time increased up to 30 s, following the expected trend ~$1/\sqrt{t}$, pointing out that the main contribution to photodetector's noise was due to the QTF thermal noise. For integration times longer than 100 s, the noise started to deteriorate. This behaviour was ascribed to

mechanical instabilities of the sensor, i.e., laser instability, mechanical vibrations, etc. which affect the performance of the sensor at long integration times.

DISCUSSION

In this work, we report on the first realization of *Black Quartz* through ultra-fast laser surface texturing aimed at extending the optical absorption of the crystal for wavelengths shorter than 5 µm. The approach consisted of designing squared matrices of ablated craters on a 250 µm thick quartz wafer. Seven different matrices were realized at fixed laser fluence *F* and repetition frequency f_R, while varying both the number of laser pulses *N* and the craters center-to-center distance *h*. A decrease in the material transmittance *T* related both to the density and the depth of the craters was found in the transparent region of pristine quartz. The two most performant matrices were applied to two identical QTFs and used as photodetector in a TDLAS setup. First, it was verified that the laser texturing did not alter the electrical properties of the two QTFs: the resonance curves of both QTFs were compared before and after the laser texturing and negligible deterioration of the *Q* value was verified. Then, the two QTFs were mounted in a TDLAS setup to detect two water absorption features, one at 1.39 µm and another one at 7.39 µm. The tests clearly demonstrated that the laser texturing enabled the infrared optical absorption in the transparent region, without impacting on the performance in the opaque region, providing an efficient extension of the optical absorption from near to mid infrared range up to 10 µm.

This work represents a starting point for future developments of *Black Quartz*. Other surface texturing patterns different from crater-matrix layout could be now investigated, like e.g. continuous texturing over a more extended area or crossed grooves, to stimulate a comprehensive study on the dependence of the optical absorption on the surface topography. Moreover, further studies could be conducted on the optimization of the QTF design for relating the thermoelastic conversion and the piezoelectric charge generation with the dimension and the position of the microstructures, with the aim at improving the responsivity of a QTF-based infrared photodetector.

Materials and methods

Experimental apparatus

The experimental setup used to perform the laser texturing of quartz wafers and QTFs is shown in Fig. 6.

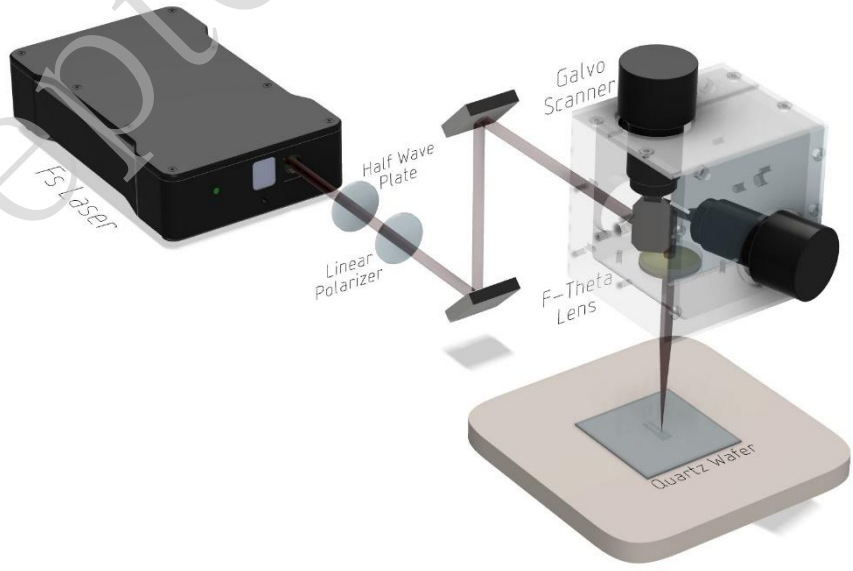

Fig. 6. Schematic representation of the apparatus for superficial laser-texturing of quartz wafer.

The quartz wafers were provided by Nano Quartz Wafer GmbH. They consisted in double polished z-cut quartz wafers with an extension of 24.5 x 24.5 mm^2 and a thickness of 250 µm. The employed laser source was a Pharos SP 1.5 from Light Conversion. This source emitted laser pulses whose temporal duration was tuneable from 190 fs to 10 ps. The emitted beam was centred at a wavelength of 1030 nm with a Gaussian-like profile with M^2 = 1.3. The maximum average laser power was 6 W corresponding to a maximum pulse energy of 1.5 mJ. The repetition frequency f_R was tuneable from single pulse to 1 MHz. The laser beam was emitted from the source with linear polarization. A half-wave plate and a polarizer were coupled to fine tune the laser beam power. The linear polarizer transmitted the P-component of polarization. The laser beam was directed to a PC-controlled galvo scanner SCANLAB intelliSCAN$_{SE}$ 14 coupled with a 100 mm F-theta lens. The estimated laser diameter in air was 28 µm. The samples were placed in the focal plane of the F-theta lens.
The samples were imaged using an optical microscope (Nikon Eclipse E600). A Scanning-Electron-Microscope (SEM) from Zeiss (Mod Sigma, Germany) was employed to perform an energy-dispersive x-ray analysis (EDX).

Responsivity calculation

When a monochromatic radiation at optical frequency ν, modulated at a mechanical frequency *f*, hits an infrared photodetector, the spectral responsivity can be expressed as:

$$R(\nu, f) = \frac{S(nf)}{\Delta P_{nf}(\upsilon)} \quad (1)$$

where *S(nf)* is the photodetector signal demodulated at *f* or one of its subharmonics (*nf*, with *n* = 2,3…) and ΔP_{nf} is the amplitude of the power modulation. In *2f*-WM and derivative spectroscopy, the *2f*-WM peak signal can be approximated as:

$$\Delta P_{2f} = \frac{P_0}{4}\alpha''(\upsilon_0)\Delta\upsilon^2 L \quad (2)$$

where $\alpha''(\nu_0)$ is the second derivative of the absorption coefficient and ν_0 is the peak frequency of the absorption coefficient.[54] Assuming a Lorentzian lineshape, the second derivative in $\nu = \nu_0$ is:

$$\alpha''(\upsilon_0) = \frac{2\sigma(\upsilon_0)Nc}{\gamma^2} \quad (3)$$

where $\sigma(\nu_0)$ is the absorption cross section at the absorption peak, as provided by the HITRAN database, *c* is the water concentration in air, γ is the half-width at half-maximum of the Lorentzian line, and *N* the molecular density, that can be related to thermodynamic parameters by the ideal gas law approximation. In the TDLAS with *2f*-WM detection, the peak signal of the 2f-absorption feature is maximized when the modulation depth $\Delta\nu \sim \gamma$. With this assumption, the responsivity $R(\nu_0, 2f)$ becomes:

$$R(\nu_0, 2f) = \frac{S(2f)}{\frac{P_0}{2}\sigma(\upsilon_0)NcL} \quad (4)$$

Both temperature (*T*) and relative humidity (*RH*) values are used to calculate the absolute water concentration in air in %-unit using the following equations:

$$c = 10^2 \frac{P_w}{P - P_w} \quad (5)$$

$$P_w = P_{ws}\frac{RH}{100} \tag{6}$$

$$P_{ws} = 6.11 \cdot e^{\frac{17.7 \cdot T}{T+243.57\,°C}} \tag{7}$$

where P is the ambient pressure (760 Torr), P_w is the water vapor pressure, and P_{ws} is the saturated water vapor pressure. With T = 19 °C and RH = 50 %, the water concentration results c = 1.4%.

Equivalent circuit of a quartz tuning fork

The Butterworth–Van Dyke model is largely used to simulate the electrical behavior of a QTF. However, to simplify the overall transfer function at the output signal of the QTF, the Butterworth–Van Dyke model can be replaced by its equivalent Norton model, according to the scheme shown in Fig. 7.

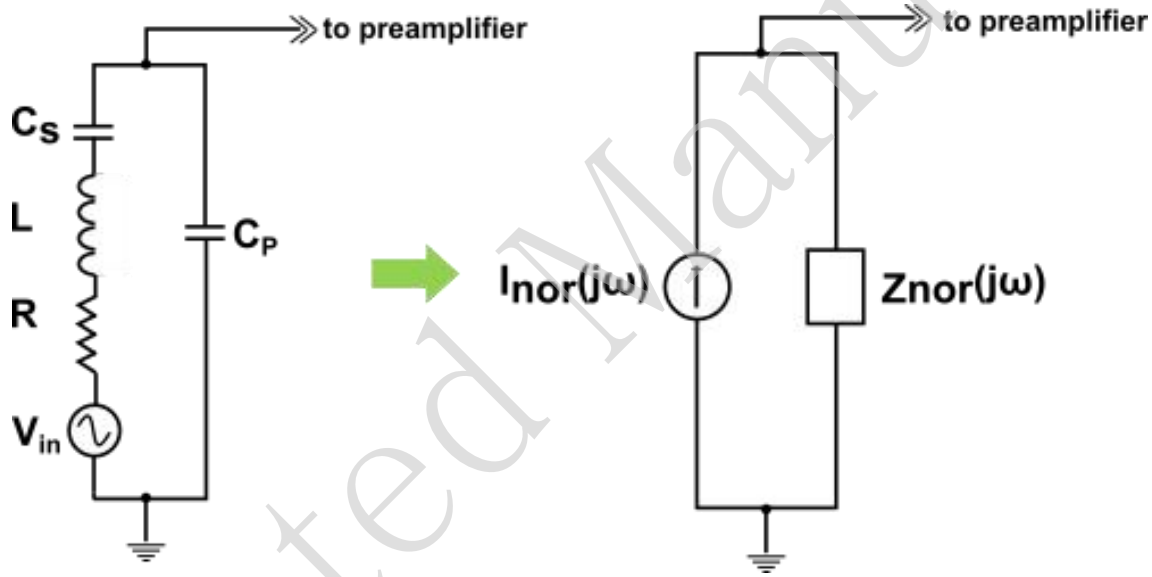

Fig. 7. (a)The Butterworth–Van Dyke model of the QTF. (b) Norton equivalent model of the QTF. $I_{nor}(j\omega)$ is the equivalent current and $Z_{nor}(j\omega)$ the impedance of the QTF.

The QTF is represented as the parallel connection between an equivalent current source $I_{nor}(j\omega)$ and the impedance $Z_{nor}(j\omega)$ of the QTF, where $\omega = 2\pi f$. $I_{nor}(j\omega)$ is the current that flows between the QTF pins if they are short-circuited and its expression can be easily derived as:

$$I_{nor}(j\omega) = V_{in} \cdot \frac{j\omega C_s}{(1-\omega^2 LC_s) + j\omega RC_s} \tag{8}$$

where V_{in} is the excitation voltage and R, C_s and L are the resistance, the capacitance and the inductance of the Butterworth–Van Dyke model of the QTF, respectively. The series-resonant frequency f_S of the QTF can be calculated as a function of its electrical parameters:

$$f_S = \frac{\omega_S}{2\pi} = \frac{1}{2\pi\sqrt{LC_S}} \tag{9}$$

as well as its quality factor *Q*:

$$Q = \frac{1}{\omega_S R C_S} \tag{10}$$

Thus, a scan of the excitation angular frequency ω nearby the series-resonant angular frequency ω_S allows the reconstruction of the spectral response of the QTF. Then, the resonance frequency and the quality factor can be easily retrieved by extracting the peak value f_0 and the full-width at half-maximum value Δf of the Lorentzian fit of the curve, respectively, being $Q = f_0/\Delta f$.

Allan-Werle deviation analysis

The minimum detection limit represents the most important figure of merit of any gas sensor, since it corresponds to the gas concentration providing a signal-to-noise ratio equal to 1. Thus, its calculation passes though the estimation of the noise level, which is usually measured as the 1σ deviation of a set of signals acquired with an integration time τ, with the laser locked on the absorption peak and fixed conditions imposed in the absorption cell. It goes without saying that the noise level, and so the minimum detection limit of a sensor, can be improved by further increasing τ. Theoretically, the signal from a perfectly stable system could be infinitely averaged; however, a sensor is a limited-stable system. At longer averaging times, drift effects usually deteriorate the performance of an optical sensor, mainly caused by additional noise contributions, like laser instability, temperature and mechanical drifts, as well as moving optical fringes, which can start to dominate at different timescales. For this reason, an optimum integration time which minimizes the noise level of a sensor can be found. The reconstruction of the trend of the noise level as a function of τ by varying step-by-step the signal integration time is unfeasible because time-consuming. For this reason, an Allan deviation analysis was performed to simulate the noise level trend at different integration times starting from a set of time-series data acquired with a fixed integration time τ_0. Given a set of N time-series data acquired with an integration time τ_0, its Allan variance $\sigma^2_y(\tau_0)$ is defined as

$$\sigma_y^2(\tau_0) = \frac{1}{N}\sum_{k=1}^{N}\frac{1}{2}(y_{k+1} - y_k) \tag{11}$$

where y_k is the k^{th} data averaged over an integration time τ_0, and y_{k+1} and y_k are adjacent values. To simulate σ^2_y at longer integration times $\tau > \tau_0$, a simple algorithm has been developed in LabVIEW. Assuming that there is no dead time between adjacent measurements, the software averages the values for y_1 and y_2 and obtains a new y_1-value averaged over $2\tau_0$. Subsequently, this routine applies the same procedure for the subsequent couples of data to obtain a new time-series data corresponding to an integration time $2\tau_0$. Finally, Eq. (11) is applied to this new set of time-series data to determine $\sigma^2_y(2\tau_0)$. The software loops this process for all other integer multiples n of τ_0 to generate values for $\sigma^2_y(n\tau_0)$ as a function of $(n\tau_0)$. The obtained trend can be used to identify the main noise contributions of a sensor, when possible. In the case of a QTF, the main noise component is expected to be the thermal noise:

$$\sigma_{thermal} = \sqrt{\frac{2k_B T}{\pi R \tau}} \tag{12}$$

where k_B is the Boltzmann constant and T = 298K is the QTF temperature. Thus, if the QTF thermal noise is the dominant noise source in a certain timescale for a QTF-based photodetector in a TDLAS setup, the Allan

deviation is expected to follow a $1/V\tau$ dependence in that timescale. If the Allan deviation deviates from this trend, other contributions are deteriorating the overall noise level of the sensor.

ACKNOWLEDGEMENTS

The authors from Dipartimento Interateneo di Fisica di Bari acknowledge financial support from PNRR MUR project PE0000023-NQSTI, project MUR – Dipartimenti di Eccellenza 2023–2027 – Quantum Sensing and Modelling for One-Health (QuaSiModO) and THORLABS GmbH within the PolySenSe joint research laboratory. The authors from Shanxi University acknowledge financial support from National Natural Science Foundation of China (NSFC) under grant number 62122045, 62235010, 62175137, 62105252 and the Shanxi Science Fund for Distinguished Young Scholars (20210302121003).

CONFLICT OF INTEREST

The authors declare no conflict of interest to disclose.

AUTHOR CONTRIBUTION

R.D. and A.V. performed the laser texturing. R.D. and A.Z. performed the optical and spectroscopical characterization experiments. R.D., P.P., A.V., A.S., A.A. contributed to data analysis. P.P, A.V., A.A., H.W and V.S. supervised the project. All authors contributed to preparing the manuscript.

DATA AVAILABILITY

The authors declare that all data supporting the findings of this study can be found within the paper and its Supplementary information files. Additional data supporting the findings of this study are available from the corresponding authors (V.S., A.V., H.W.) upon reasonable request.

REFERENCES

1. Melchior, H., Fisher, M. B. & Arams, F. R. Photodetectors for optical communication systems. *Proceedings of the IEEE* **58**, 1466-1486 (1970).
2. Tan, C. L. & Mohseni, H. Emerging technologies for high performance infrared detectors. *Nanophotonics* **7**, 169-197 (2018).
3. Rogalski, A. Infrared detectors: an overview. *Infrared Physics & Technology* **43**, 187-210 (2002).
4. Wen, Z. Y. et al. Broadband up‐conversion mid‐infrared time‐stretch spectroscopy. *Laser & Photonics Reviews* **18**, 2300630 (2024).
5. Hashemi Amiri, S. E. et al. Growth of InGaAsP alloy nanowires for emission from visible to mid-infrared wavelengths. *ECS Meeting Abstracts* **MA2015-02**, 1174 (2015).
6. Katzir, E. et al. Tunable inkjet printed hybrid carbon nanotubes/nanocrystals light sensor. *Sensors and Actuators B: Chemical* **196**, 112-116 (2014).
7. Lou, Z. & Shen, G. Z. Flexible photodetectors based on 1D inorganic nanostructures. *Advanced Science* **3**, 1500287 (2016).
8. Wu, E. P. et al. In situ fabrication of 2D WS_2/Si type-ii heterojunction for self-powered broadband photodetector with response up to mid-infrared. *ACS Photonics* **6**, 565-572 (2019).
9. Dong, T., Simões, J. & Yang, Z. C. Flexible photodetector based on 2D materials: processing, architectures, and applications. *Advanced Materials Interfaces* **7**, 1901657 (2020).
10. Mak, K. F. et al. Optical spectroscopy of graphene: from the far infrared to the ultraviolet. *Solid State Communications* **152**, 1341-1349 (2012).
11. Liu, C. H. et al. Graphene photodetectors with ultra-broadband and high responsivity at room temperature. *Nature Nanotechnology* **9**, 273-278 (2014).
12. Gattass, R. R. & Mazur, E. Femtosecond laser micromachining in transparent materials. *Nature Photonics* **2**, 219-225 (2008).
13. Balling, P. & Schou, J. Femtosecond-laser ablation dynamics of dielectrics: basics and applications for thin films. *Reports on Progress in Physics* **76**, 036502 (2013).
14. Mur, J. et al. Ultra-fast laser-based surface engineering of conductive thin films. *Applied Surface Science* **509**, 144911 (2020).
15. Sfregola, F.A. et al. Influence of working parameters on multi-shot femtosecond laser surface ablation of lithium niobate. *Optics & Laser Technology* **177**, 111067 (2024).
16. Shin, H. & Kim, D. Cutting thin glass by femtosecond laser ablation. *Optics & Laser Technology* **102**, 1-11 (2018).
17. Her, T. H. et al. Microstructuring of silicon with femtosecond laser pulses. *Applied Physics Letters* **73**, 1673-1675 (1998).
18. Wu, C. et al. Near-unity below-band-gap absorption by microstructured silicon. *Applied Physics Letters* **78**, 1850-1852 (2001).
19. Bonse, J. et al. Femtosecond laser ablation of silicon-modification thresholds and morphology. *Applied Physics A* **74**, 19-25 (2002).

20. Halbwax, M. et al. Micro and nano-structuration of silicon by femtosecond laser: Application to silicon photovoltaic cells fabrication. *Thin Solid Films* **516**, 6791-6795 (2008).

21. Jiang, J. et al. Mechanism of optical absorption enhancement of surface textured black silicon. *Journal of Materials Science: Materials in Electronics* **24**, 463-466 (2013).

22. Liu, H. et al. Micro/nanostructures for light trapping in monocrystalline silicon solar cells. *Journal of Nanomaterials* **2022**, 8139174 (2022).

23. Sun, H. B. et al. Mid-long wavelength infrared absorptance of hyperdoped silicon via femtosecond laser microstructuring. *Optics Express* **30**, 1808-1817 (2022).

24. Wang, M. et al. Mid-and far-infrared localized surface plasmon resonances in chalcogen-hyperdoped silicon. *Nanoscale* **14**, 2826-2836 (2022).

25. Tansel, T. & Aydin, O. Long infrared detector based on Se-hyperdoped black silicon. *Journal of Physics D: Applied Physics* **57**, 295103 (2024).

26. Phillips, K. C. et al. Ultrafast laser processing of materials: a review. *Advances in Optics and Photonics* **7**, 684-712 (2015).

27. Liu, X. G. et al. Black silicon: fabrication methods, properties and solar energy applications. *Energy & Environmental Science* **7**, 3223-3263 (2014).

28. Liu, X. L. et al. Perspectives on black silicon in semiconductor manufacturing: Experimental comparison of plasma etching, MACE, and Fs-laser etching. *IEEE Transactions on Semiconductor Manufacturing* **35**, 504-510 (2022).

29. Calvani, P. et al. Black diamond for solar energy conversion. *Carbon* **105**, 401-407 (2016).

30. Girolami, M. et al. Impact of laser wavelength on the optical and electronic properties of black diamond. *Physica Status Solidi (A)* **214**, 1700250 (2017) doi: 10.1002/pssa.201700250.

31. Sun, J. et al. Mid-infrared gas absorption sensor based on a broadband external cavity quantum cascade laser. *Review of Scientific Instruments* **87**, 123101 (2016).

32. Ding, J. Y. et al. Quartz tuning fork-based photodetector for mid-infrared laser spectroscopy. *Applied Physics B* **124**, 78 (2018).

33. Li, J. S. et al. Piezoelectric effect-based detector for spectroscopic application. *Optics and Lasers in Engineering* **115**, 141-148 (2019).

34. Ma, Y. F. et al. Quartz-tuning-fork enhanced photothermal spectroscopy for ultra-high sensitive trace gas detection. *Optics Express* **26**, 32103-32110 (2018).

35. Lord, H. W. & Shulman, Y. A generalized dynamical theory of thermoelasticity. *Journal of the Mechanics and Physics of Solids* **15**, 299-309 (1967).

36. Green, A. E. & Lindsay, K. A. Thermoelasticity. *Journal of elasticity* **2**, 1-7 (1972).

37. Chandrasekharaiah, D. S. A generalized linear thermoelasticity theory for piezoelectric media. *Acta Mechanica* **71**, 39-49 (1988).

38. Saigusa, Y. Quartz-based piezoelectric materials. in Advanced Piezoelectric Materials 2nd edn (ed Uchino, K.) (Amsterdam: Elsevier, 2017), 197-233 doi: 10.1016/B978-0-08-102135-4.00005-9.

39. Calabrese, E. & Fowler, W. B. Electronic energy-band structure of α quartz. *Physical Review B* **18**, 2888-2896 (1978).

40. He, M. Y. et al. Fundamental infrared absorption features of α-quartz: an unpolarized single-crystal absorption infrared spectroscopic study. *Vibrational Spectroscopy* **101**, 52-63 (2019).

41. Girolami, M. et al. Femtosecond-laser nanostructuring of black diamond films under different gas environments. *Materials* **13**, 5761 (2020) doi: 10. 3390/ma13245761.

42. Ashkenasi, D. et al. Laser processing of sapphire with picosecond and sub-picosecond pulses. *Applied Surface Science* **120**, 65-80 (1997).

43. Santhosh, S. et al. Effect of ablation rate on the microstructure and electrochromic properties of pulsed-laser-deposited molybdenum oxide thin films. *Langmuir* **33**, 19-33 (2017).

44. Gao, Y. C. et al. First-principles research on mechanism of sub-band absorption of amorphous silicon induced by ultrafast laser irradiation. *Results in Physics* **31**, 104941 (2021).

45. Vorobyev, A. Y. & Guo, C. L. Direct creation of black silicon using femtosecond laser pulses. *Applied Surface Science* **257**, 7291-7294 (2011).

46. Amalathas, A. P. & Alkaisi, M. M. Nanostructures for light trapping in thin film solar cells. *Micromachines* **10**, 619 (2019).

47. De Palo, R. et al. Threshold fluence and incubation during multi-pulse ultrafast laser ablation of quartz. *Optics Express* **30**, 44908-44917 (2022).

48. Heaney, J. B., Stewart, K. P. & Hass, G. Transmittance and reflectance of crystalline quartz and high- and low-water content fused silica from 2 *μ*m to 1 mm. *Applied Optics* **22**, 4069-4072 (1983).

49. Lin, H. Y. et al. Application of standard and custom quartz tuning forks for quartz-enhanced photoacoustic spectroscopy gas sensing. *Applied Spectroscopy Reviews* **58**, 562-584 (2023).

50. Hu, L. E. et al. Compact all-fiber light-induced thermoelastic spectroscopy for gas sensing. *Optics Letters* **45**, 1894-1897 (2020).

51. Olivieri, M. et al. Influence of air pressure on the resonance properties of a T-shaped quartz tuning fork coupled with resonator tubes. *Applied Sciences* **11**, 7974 (2021).

52. Hao, Z. L., Erbil, A. & Ayazi, F. An analytical model for support loss in micromachined beam resonators with in-plane flexural vibrations. *Sensors and Actuators A: Physical* **109**, 156-164 (2003).

53. Giglio, M. et al. Allan deviation plot as a tool for quartz-enhanced photoacoustic sensors noise analysis. *IEEE Transactions on Ultrasonics*, *Ferroelectrics*, *and Frequency Control* **63**, 555-560 (2016).

54. Patimisco, P. et al. Purely wavelength- and amplitude-modulated quartz-enhanced photoacoustic spectroscopy. *Optics Express* **24**, 25943-25954 (2016).